Article:
Jeannin, M, Bonazzi, T, Gacemi, D et al. (7 more authors) (2020) High temperature metamaterial terahertz quantum detector. Applied Physics Letters, 117 (25). 251102. ISSN 0003-6951

https://doi.org/10.1063/5.0033367

Supplementary Information

High temperature metamaterial TeraHertz quantum detector

Mathieu Jeannin,[1] Thomas Bonazzi,[1] Djamal Gacemi,[1] Angela Vasanelli,[1] Stéphan Suffit[2], Lianhe Li, [3]Alexander Giles Davies,[3]Edmund Linfield,[3] Carlo Sirtori[1] and Yanko Todorov[1*]

[1]Laboratoire de Physique de l'Ecole Normale Supérieure, ENS, Paris Sciences et Lettres, CNRS, Université de Paris, 24 Rue Lhomond, 75005 Paris, France

[2]Laboratoire Matériaux et Phénomènes Quantiques, Université de Paris, CNRS, 75013 Paris, France

[3]School of Electronics and Electrical Engineering, University of Leeds, LS2 9JT Leeds, United Kingdom

1. Sample fabrication

The fabrication procedure closely resembles the one described in Refs. [1, 2], but has been adapted to improve the optical quality of the sample while coping with the high temperature annealings necessary to obtain ohmic contacts between the active region and the metallic parts.

We first fabricate the *LC* resonators. We start by fabricating the 1.5x1.5 µm² ohmic contact pads below the bottom (square) capacitor plates of the LC circuits using electron beam lithography (EBL) and electron beam evaporation (EBE) of a stack of Pd/Ge/Ti/Au (15/45/5/15 nm). Using a subsequent EBL step, we pattern the bottom part of the LC circuit consisting of two capacitor plates on top of the ohmic contacts, and the straight wire connecting the two pads. We also pattern the metallic leads (long vertical wires in Fig. 1 of the main text) and evaporate a Ti/Au (5/150 nm) stack. Large contacting pads overlapping the vertical metallic leads are added using optical lithography to allow contacting the bottom side of individual arrays using wirebonding. The sample is then etched using the metal as a mask using a Cl-based inductively coupled plasma reactive ion etching (ICP-RIE). A 3 µm thick SiN insulation layer is deposited using a low temperature (150°C) plasma enhanced chemical vapor deposition (LT-PECVD) and coated with Ti/Au (10/200 nm). The sample is then flipped and bonded to a host GaAs substrate using an epoxy. The substrate is selectively etched, revealing the unprocessed side of the active region. We repeat the same two-step EBL+EBE procedure to fabricate the top contacts of the LC circuits (1.5x1.5 µm² Pd/Ge/Ti/Au pads) and then the top part of the LC circuit (Ti/Au capacitor plates, inductive loop and metallic leads). A second contacting pad is processed using optical lithography to allow contacting the top side of individual arrays. The excess active region is then removed using ICP-RIE again, revealing the metallic wires and pads buried below the active region. After this etch step, only the active region embedded in the capacitors of the LC circuits is left in the sample. Finally, a 500nm thick SiN layer is added to the sample using LT-PECVD, and the λ/2 antennas are patterned using EBL and deposited using EBE (Ti/Au 5/150nm). The SiN layer above the contact pads is then selectively removed using optical lithography and fluoride based reactive ion etching. Ultimately, the sample is annealed at 200°C on a hotplate for 30 min.

We summarize below the electrical area of each device and compare it to the physical footprint on the sample.

	La = 7µm	La = 8 µm	La = 9 µm	La = 10 µm	La = 11 µm
Footprint (µm²)	2.32 10^4	2.24 10^4	2.16 10^4	2.08 10^4	2 10^4
P = 9 µm	**2916**	**2430**	**2268**	**1944**	**1782**
P = 8 µm	**3098.25**	**2581.875**	**2409.75**	**2065.5**	**1893.375**
P = 4 µm	**2754**	**2409.75**	**2237.625**	**2065.5**	**1721.25**
P = 3 µm	**3280.5**	**2733.75**	**2551.5**	**2187**	**2004.75**
P = 2.4 µm	**3280.5**	**2916**	**2551.5**	**2187**	**2004.75**

Table S1: Electrical area (bold numbers, in µm²) of each array, and the corresponding footprint on the sample (second line).

For the reference mesa device we use standard fabrication protocol, where a top PdGe contact is defined as above. The mesa is then defined by wet etching down to the bottom n++ contact, and then we evaporate AuGeNi contacts laterally to the mesa. The lateral contacts are diffused in order to reach the bottom n++ layer.

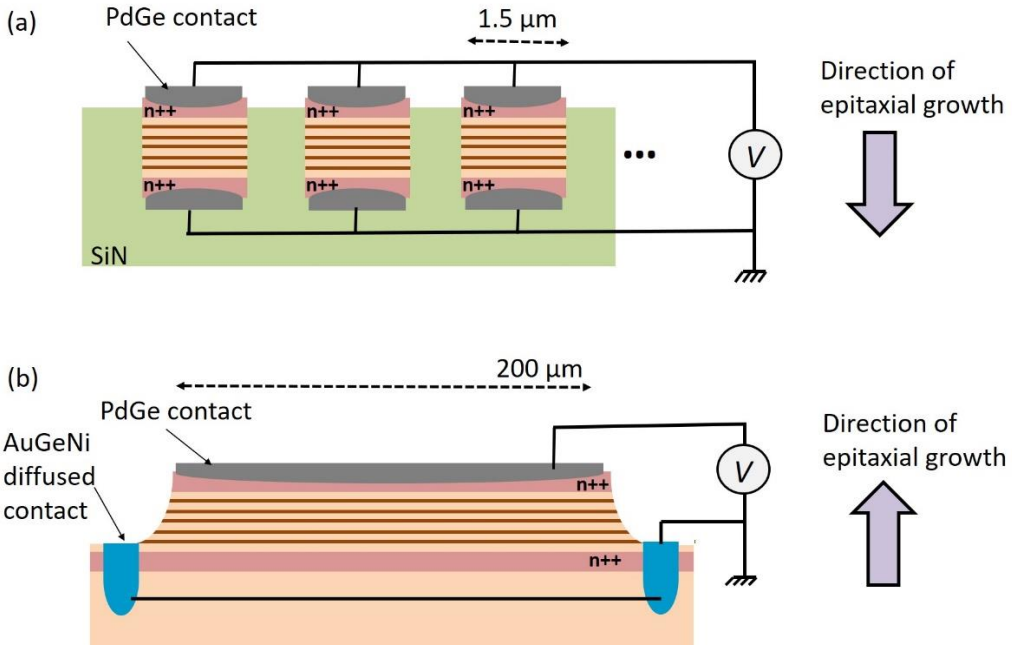

Figure S1: Illustration of the biasing scheme for the metamaterial device (a) and the mesa device (b) with respect to direction of the epitaxial growth. These illustrations are not on scale.

In Figure S1 we illustrate the electrical bias scheme for both the metamaterial and mesa device as a result of this process. Note that the as a result of the process, the absorbing region is inverted in the case of metamaterial devices with respect to the mesa device; we therefore compare the two devices for opposite sign of the applied bias. This comparison allows to take into account the asymmetries introduced by the epitaxial growth, such as dopant segregation [3].

2. Reflectivity curves

In Ref. [2] we have discussed in details the coupling between the LC resonators and the antenna elements. This coupling is described in terms of the temporal coupled mode theory [4], where the LC resonator and the antenna are treated as two coupled oscillators described by their frequencies, radiative and non-radiative loss rates: respectively (ω_{LC}, Γ_{LC}, γ_{LC}) and (ω_A, Γ_A, γ_A). The coupled-mode theory equations read:

(S1) $$\frac{da}{dt} - (i\omega_{LC} - \gamma_{LC} - \Gamma_{LC})a - iGA = \sqrt{2\Gamma_{LC}}S_{in}$$

(S2) $$\frac{dA}{dt} - (i\omega_A - \Gamma_A - \gamma_A)A - iGa = \sqrt{2\Gamma_A}S_{in}$$

(S3) $$S_{out} = -S_{in} + \sqrt{2\Gamma_A}A + \sqrt{2\Gamma_{LC}}a$$

Here a and A are the amplitudes of the LC resonator and the antenna mode; S_{in} and S_{out} are respectively the amplitude of the incident and reflected wave. The LC-antenna coupling is described by the coupling constant G. By solving the system (S1-S3) for a harmonic regime where all amplitudes evolve as $\sim e^{i\omega t}$, we obtain the reflectivity $R(\omega) = |S_{out}|^2/|S_{in}|^2$ as illustrated in Figure 2 in the main text.

The system (S1-S3) includes several parameters that have to be determined experimentally. For this we use our prior results from Ref. [4] which are supplemented with novel measurements. First, we have prepared large area arrays with an antenna length L_a=13µm and a variable perimeter P. The resulting reflectivity spectra at room temperature and their modelling through the system (S1-S3) are shown in Figure S2.

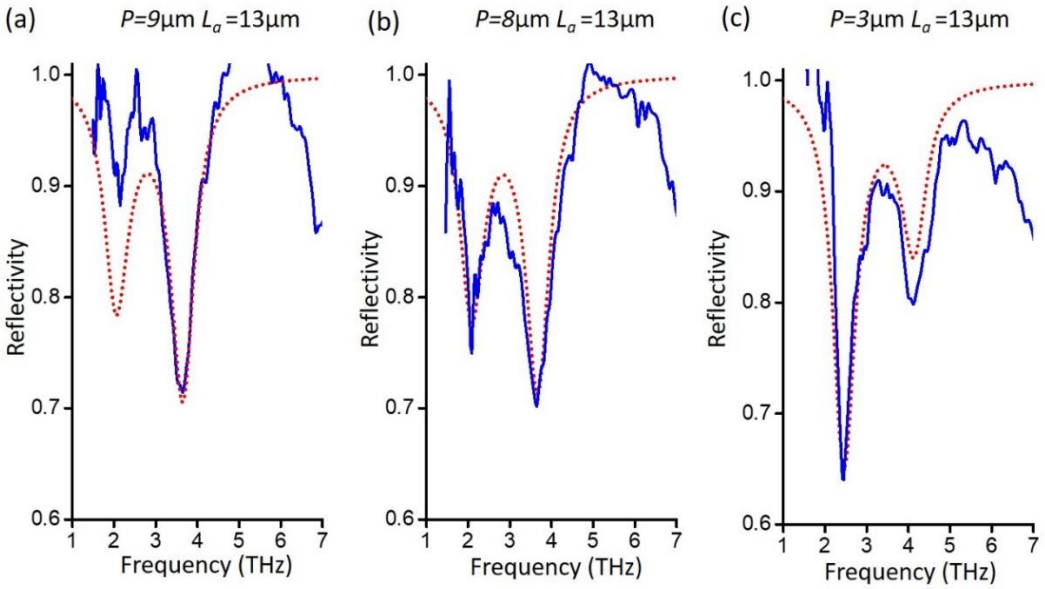

Figure S2: Reflectivity spectra at room temperature of large area (~1 mm²) arrays comprising L_a = 13 µm long antennas and LC resonators with variable perimeter P: (*a*) P = 9 µm, (*b*) P = 8 µm and (*c*) P = 3 µm. The full blue curves are experimental results and the dotted curves are modelling from the equations (S1-S3).

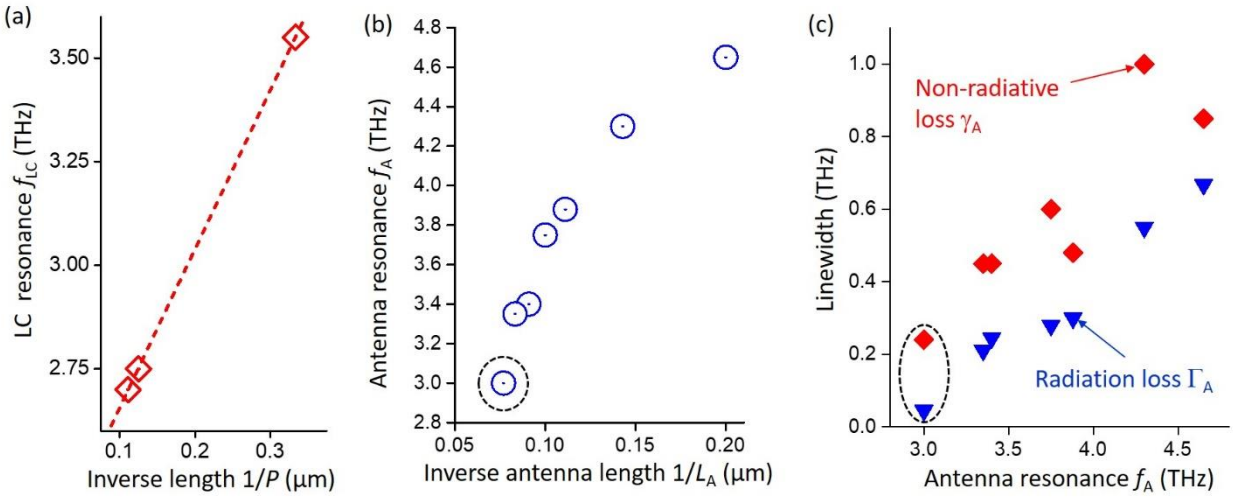

Figure S3: (a) LC resonant frequencies ($f_{LC}=\omega_{LC}/2\pi$, in THz) as a function of the inverse perimeter (1/P, in μm), as extracted from the data modelling of the data in Figure S2. (b) Resonant frequencies of the antennas ($f_A=\omega_A/2\pi$, in THz) obtained from the data in Ref. [2] and the data from Figure S1 (dot in dashed circle). (c) Non radiative (γ_A, diamonds) and radiative loss rates (Γ_A, triangles) obtained from Ref. [2] and the data from Figure S2 (symbols in dashed ellipse).

From these measurements we extract the various parameters such as the resonant frequencies of the uncoupled LC resonator (Figure S3(a)), as well as the magnitude of the coupling parameter G = -0.8 THz. As in Ref. [2] we found that the radiation loss Γ_{LC} of the LC structures are negligeable, and they have non-radiative linewidth of γ_{LC}=0.4 THz. By studying uncoupled LC resonators alone, we found that the annealing of the ohmic contacts introduces a frequency shift Δf_{LC}=+0.56 THz that is taken into account in the final modelling shown in Figure 2. For the P = 4 μm we find thus that the resonant frequency of the LC resonator alone is f_{LC} = 3.8 THz.

The fit parameters from the data of Figure S1 are combined with the results from Ref. [2] to obtain all characteristics of the wire antennas (Figure S3(b,c)). In particular, we found the following values: f_A = 4.3 THz for L_a=7 μm, f_A = 4.07 THz for L_a=8 μm, and f_A = 3.7 THz for L_a=10 μm. For all antennas we use the parameters γ_a=0.45 THz and Γ_A= 0.32 THz.

3. Dark current fits

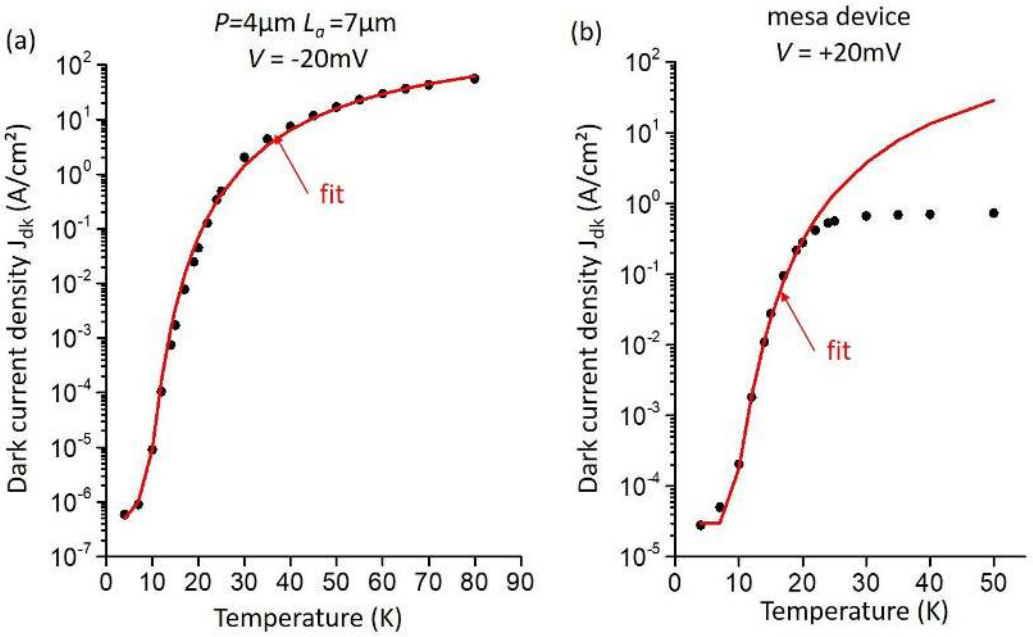

Figure S4: (a) Dark current density as a function of the temperature for the metamaterial device *P= 4* µm and L_a = 7 µm biased at -20 mV. The dots are experimental data and the full line is exponential fit. (b) The corresponding data for the mesa device.

The temperature activated dark current is fitted with the function $J_{dark} = J_0 \exp(-E_{act}/k_B T) + const$, as shown in Figure S4. The parameters for the metamaterial device (a) are J_0 = 2.8 A/cm², E_{act} = 15.6 meV and *const* = 5.9x10^{-7} A/cm². For the mesa the corresponding parameters are: J_0 = 600 A/cm², E_{act} = 13.1 meV and *const* = 3x10^{-5} A/cm². For the mesa, the deviation at high temperature can be explained by an extra resistance R ~ 10kΩ in series with the device R_{device}, such as the total resistance is R+R_{device}. At low temperature, the device is very resistive, R_{device} ~ 100 MΩ, meaning that the effect of R is negligeable. At high temperature, we expect the device to have an intrinsic resistance on the order of R_{device} ~ 1Ω, and therefore we see essentially the effect of *R*. The most probable explanation for the presence of *R* in for the case of the mesa is as follows. As illustrated in Fig. S1(a) for the mesa devices we use lateral bottom contact, with very thin, 40 nm, contact layer. Because of the very thin contact layers over a very large area mesa 200 µm x 200 µm we could expect an extra lateral resistance *R* in series with the resistance QW region. Note that we do not observe current saturation for the metamaterial detectors, even if the high temperature resistance is R_{device} ~ 10 Ω. Indeed, in the case of metamaterials the QW are contacted with metal contacts on both sides, and furthermore the lateral sizes of the pads are 1.5 µm, which removes completely any effect of any lateral resistance (Fig. S1 (a)).

4. Photocurrent and responsivity measurements

In order to determine the responsivity of our devices we have used calibrated black body source heated at 500°C and a lock-in amplifier. Details of the experimental set-up are provided in Figure S5 (a). The blackbody radiation is focused on the sample with a help of a F1 parabolic mirror, after passing on a 50% mechanical chopper rotating at a speed 120 Hz. The current from the sample is amplified with a low-noise transimpedance amplifier and then send to the lock-in amplifier. The photocurrent

I_{ph} is related to the lock-in reading $V_{lock\text{-}in}$ through the formula $I_{ph} = V_{lock\text{-}in}(\pi/2^{1/2})/g_{tr}$, where g_{tr} is the transimpedance gain.

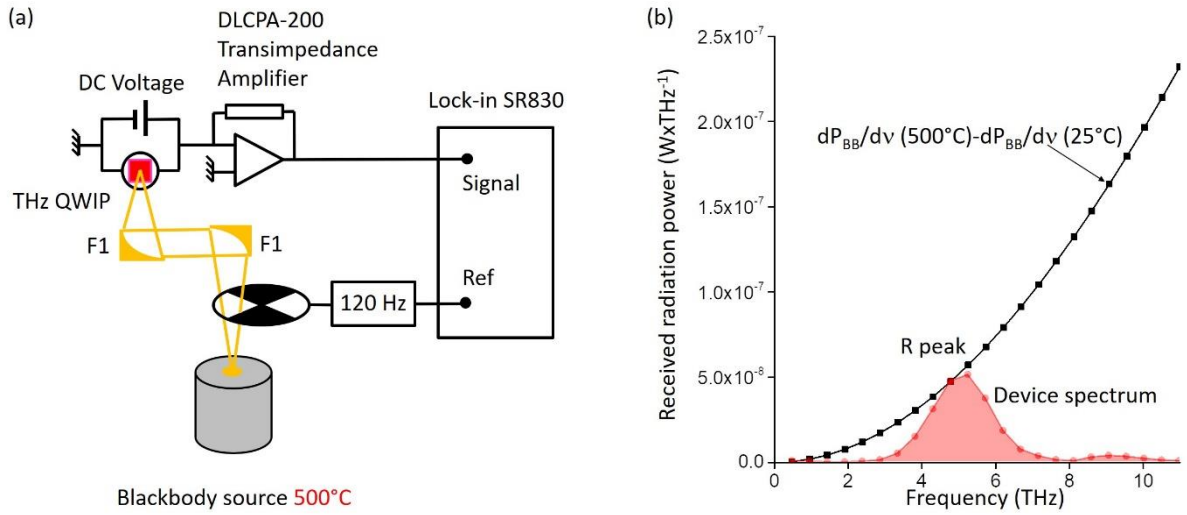

Figure S5: (a) Full experimental set-up for the measurements of the device responsivity. (b) Estimate of the received radiation power on the device. The black curve is a difference between 500°C and 25°C blackbody sources. The device spectrum has been normalized such as its maximum is set on the black curve. The resulting curve corresponds exactly to the integrand in Eq. (S5).

As we use a broadband source the measured photocurrent I_{ph} corresponds to total signal collected from the entire spectral range of our THz detector. The spectral shape of the responsivity has been determined from spectrally resolved photocurrent measurements with the help of a FTIR as described in the main text and Figure 4(a). In order to obtain the correct spectral shape of the responsivity $R(\nu)$ the photocurrent spectra have been normalized on the power spectral density of the globar source of the FTIR assumed to be a blackbody of a temperature T =1200K.

Knowing the spectral shape $R(\nu)$ responsivity we can determine the absolute value of the peak responsivity R_{peak}. Responsivity can be cast in the form:

(S4) $$R(\nu) = R_{peak} L(\nu)$$

Here R_{peak} is the maximum responsivity at a frequency ν_{peak} = 5.2 THz (see Figure 4(a).) and $L(\nu)$ is the function that describes the responsivity spectrum but normalized such as $L(\nu=\nu_{peak}) = 1$. The total photocurrent measured from the lock-in experiment described above is thus provided by the formula:

(S5) $$I_{ph} = R_{peak} \int_0^{\infty} L(\nu) \left\{ \frac{dP_{BB}}{d\nu}(T = 500°C) - \frac{dP_{BB}}{d\nu}(T = 25°C) \right\} d\nu$$

Here $dP_{BB}/d\nu(T)$ is the spectral density of a black-body radiation incident on the detector that has been computed taking into account the device area and the solid angle of the F1 focusing mirror (see, for instance, equation (2.6) on page 7 from Ref. [5]). In this formula we take into account the fact that when the detector is facing the palette of the mechanical chopper it is actually exposed to the ambient

black body radiation at 300K (~25°C). The function under the integral of Eq.(S5) has been plotted in Figure S5(b) together with the expression in brackets. The total power received by the device corresponds to the red area in the graph of Figure S5(b). For instance, for metamaterial devices we have typically an incident power 220nW. From this value we determine the peak responsivities shown in Figure 4(b) in the main text.

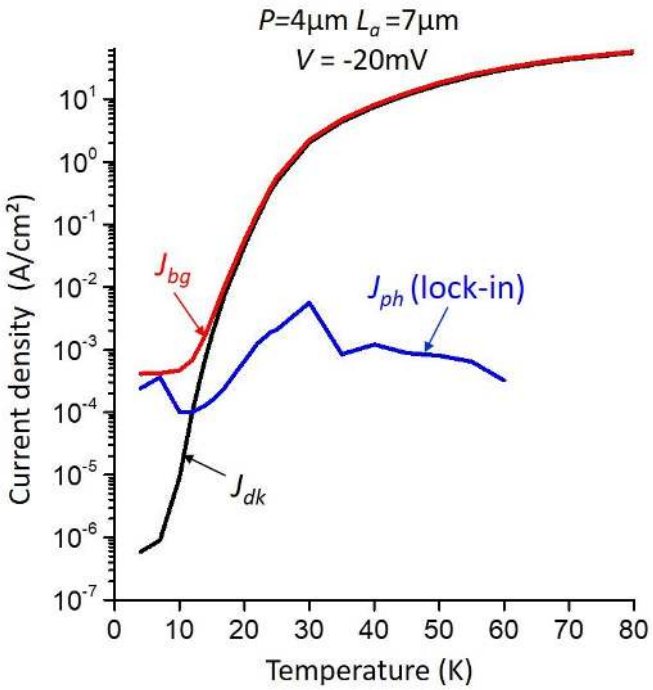

Figure S6: Comparison between current densities obtained from direct measurement of current voltage characteristics and photocurrent density measured in the lock-in experiment.

The DC measurements shown in Figure 2 of the main text were obtained with Yokogawa GS200 source/ measurement unit. In Figure S6 we show a comparison between DC current voltage characteristics and photocurrent obtained by a lock-in experiment described above. At low temperature, where the dark current is negligible we see that the background current is of the same order of magnitude as the photocurrent obtained from with the lock-in amplifier. These observations attest the reliability of our estimation for the responsivity.

5. Polarization dependence of the photoresponse

By construction the optical response of our metamaterial is dependent on the polarization of the incident THz wave. Only the electric field component of the incident wave, that is parallel to the wire antenna excites the metamaterial resonance [2]. As a consequence, the photoresponse of the detector is also dependent on the polarization of the incident polarization. This selection has been experimentally verified by placing a wiregrid THz polarizer in front of the detector, and measuring the spectral response as a function of the angle θ between the active polarization and the wire antennas of the metamaterial. These results are shown in Figure S7(a,b). As seen from Fig. S7(a) the photocurrent intensity is maximal when the incident electric field vector is aligned with the wire antennas. Furthermore, as shown in Fig. S7(b) the photocurrent signal follows the expected

$\cos^2\theta$ dependence. These results attest for the fact that the photoresponse of the device is mediated by the coupling between the metamaterial resonance and the electronic transitions, and not by any other spurious effects (i.e. bolometric effect). These measurements were performed with the (P=4µm, L_a =7µm) device.

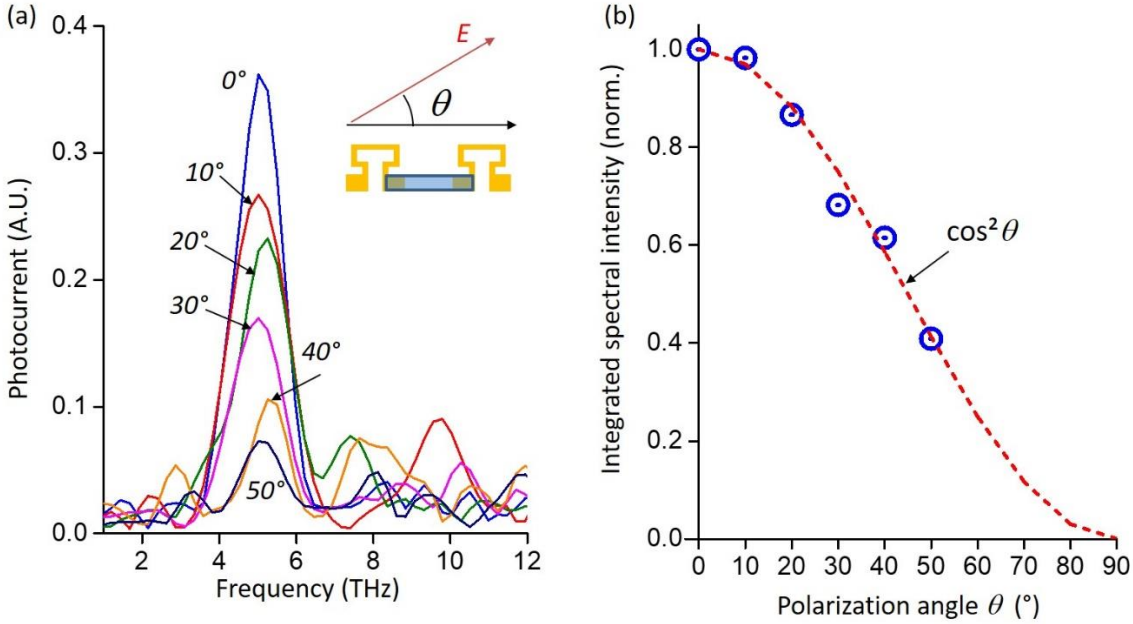

Figure S7: (a) Photocurrent spectra as a function of the polarization of the incident wave. The inset shows the electric field vector with respect to the wire antenna. In our experiments we vary the angle θ defined in the inset. (b) Values of the integrals of the photocurrent spectra as a function of θ (dots). The dashed line is a plot of the expected $\cos^2\theta$ dependence.

6. Current-voltage characteristics of all structures reported in the main text

Here we provide the current voltage characteristics of the structures (P = 4 µm, L_a = 8 µm) and (P =4 µm, L_a= 10µm) that were used to obtain the results reported in Figure 5.

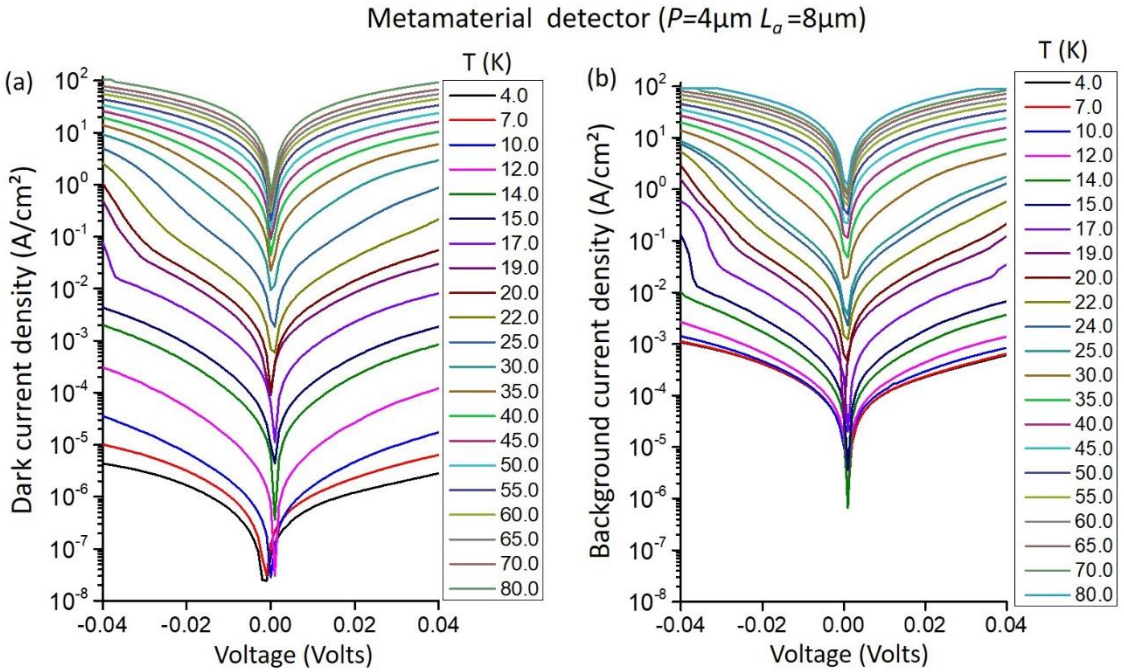

Figure S8: Current-voltage characteristics for under dark conditions (a) and background illumination (b) for the sample (*P*=4μm, L_a=8μm).

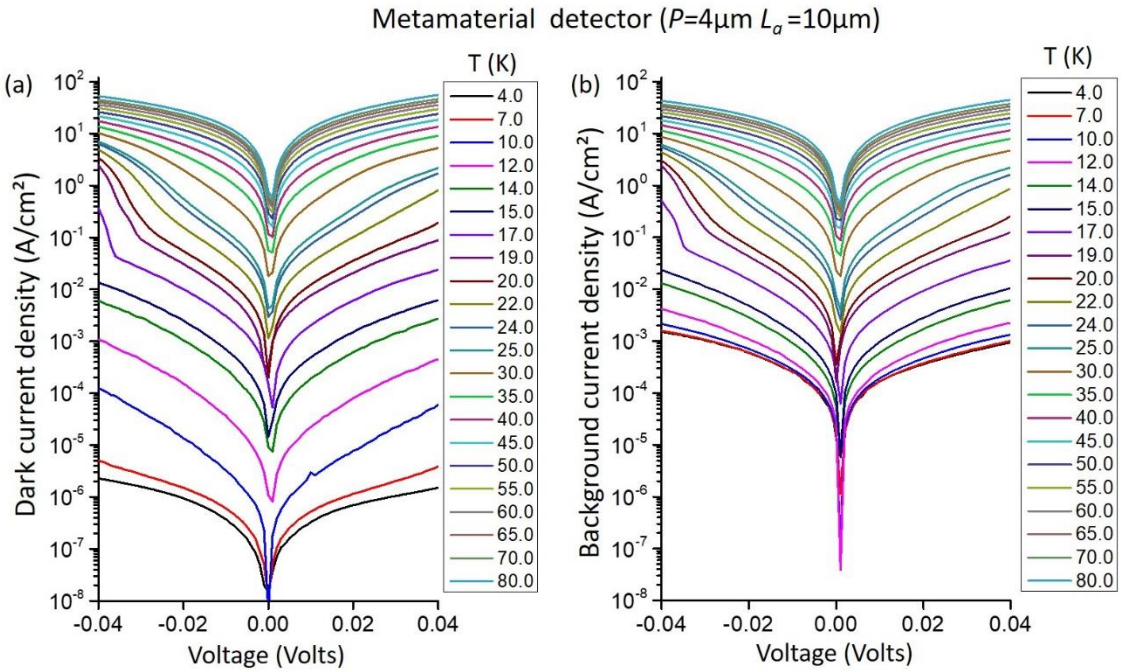

Figure S9: Current-voltage characteristics for under dark conditions (a) and background illumination (b) for the sample (*P*=4μm, L_a=10μm).

7. References

[1] M. Jeannin, G. Mariotti Nesurini, S. Suffit, D. Gacemi, A. Vasanelli, L. Li, A. G. Davies, E. Linfield, C. Sirtori, and Y. Todorov, ACS Photonics **6** (5), 1207-1215, (2019)

[2] M. Jeannin, T. Bonazzi, D. Gacemi, A. Vasanelli, L. Li, A. G. Davies, E. Linfield, C. Sirtori, and Y. Todorov. Nano Letters 20 (6) , 4430-4436 (2020). https://doi.org/10.1021/acs.nanolett.0c01217

[3] H. Schneider, E. C. Larkins, J. D. Ralston, K. Schwarz, F. Fuchs, and P. Koidl , "Space charge effects in photovoltaic double barrier quantum well infrared detectors", Applied Physics Letters **63**, 782–784, (1993)

[4] H. A. Haus, "Waves and fields in optoelectronics" Marietta, Ohio: CBLS, 2004

[5] H. Schneider and H.C. Liu, "Quantum Well Infrared Photodetectors Physics and Applications", Springer, New York United States (2007)